

Epitaxial Stabilization of $\text{Ge}_{1-x}\text{Sn}_x$ Alloys

Alfonso Sanchez-Soares,^{1,2} Conor O'Donnell,² and James C. Greer^{3,4}

¹*EOLAS Designs, Grenagh, Co. Cork, T23 AK70, Ireland*

²*Tyndall National Institute, University College Cork, Dyke Parade, Cork, T12 R5CP, Ireland*

³*Nottingham Ningbo New Materials Institute, The University of Nottingham Ningbo China, Ningbo, 315100, China*

⁴*Department of Electrical and Electronic Engineering,
The University of Nottingham Ningbo China, Ningbo, 315100, China**

The thermodynamic stability of $\text{Ge}_{1-x}\text{Sn}_x$ alloys is investigated across the full composition range by employing density functional theory (DFT) in conjunction with the cluster expansion formalism (CE). Configurational, vibrational, and electronic entropy contributions are estimated to allow computation of alloy free energy at finite temperatures. Germanium and tin are found to be immiscible in the bulk up to temperatures approaching germanium's melting point, and much higher than that of tin. Since the main contribution to alloy destabilization is found to be related to the large difference in atomic radii between atomic constituents, the possibility of stabilizing the alloy by reducing segregation through epitaxial constraints in thin films is explored. For germanium-tin alloys, the (001) substrate orientation is preferred for epitaxial growth as it allows for the largest degree of out-of-plane relaxation. Epitaxial films have been simulated by biaxially straining bulk alloy cells as to constrain their lattice spacing to that of substrates lattice-matched to $x = 0$, and approximately $x = 0.5$, and $x = 1$. We conclude that due to the large difference in elastic constants between the components, epitaxial films with high tin content grown on lattice-matched substrates exhibit the greatest stability.

I. INTRODUCTION

Germanium-tin alloys have received significant attention over the past decade due to their potential applications in optoelectronic devices. It represents the only group IV binary alloy predicted to exhibit a direct electronic band gap, making it particularly suitable for photonics devices which can be readily integrated into an industry and infrastructure dominated by silicon. Furthermore, germanium and tin are already present in electronics manufacturing processes as *technology boosters* to improve the performance of silicon-based devices; a material with such properties and level of integration into semiconductor processing presents numerous opportunities for novel electronic and optoelectronic device designs. Although silicon-germanium alloys were successfully introduced into electronics manufacturing decades ago, progress towards technological applications involving germanium-tin alloys has been much slower mainly due to two of its key characteristics: i) its constituents exhibit a large difference in ionic radii which results in a low solid solubility of tin in germanium ($\approx 1\%$) as predicted by the Hume-Rothery rules for substitutional alloys,¹ and ii) tin's stable phase under standard conditions is β -Sn (metallic; tetragonal crystal structure) instead of the preferred for electronics cubic α -Sn (semimetallic; cubic crystal structure), stable at temperatures below 13.2°C at ambient pressure.² Such characteristics result in significant difficulty in incorporating tin into germanium crystals without the formation of metallic β -Sn clusters within the alloy. Great progress has been made in past decades towards fabricating germanium-tin alloys by employing non-equilibrium epitaxial growth techniques such as molecular beam epitaxy (MBE) and chemical vapor deposition (CVD),

allowing realization of thin films with thicknesses up to hundreds of nanometers.³⁻⁶ Moreover, recent studies have reported lasers comprised of $\text{Ge}_{1-x}\text{Sn}_x$ thin films with low tin content ($0.08 < x < 0.13$), indicating significant advances towards fabrication of alloys with device-grade crystallinity.⁷⁻⁹

Although recent efforts have been focused on fabricating films with low tin content alloys for photonics applications, the electronic structure character of germanium-tin alloys has been predicted to vary significantly with composition: the addition of a few atomic percent of tin into germanium induces a transition to a direct band gap, while alloys with larger tin contents exhibiting semimetallic behavior.¹⁰ While integration of direct band gap $\text{Ge}_{1-x}\text{Sn}_x$ into electronic devices already carries great potential such as enhanced carrier mobilities, optical interconnects, and efficient designs for devices based on tunneling such as tunneling field-effect transistors (TFETs) or tunnel diodes,¹¹⁻¹³ the possibility of increasing tin composition to induce semimetallic regions or to counteract confinement-induced band gap widening in nanoelectronic device designs further increases these alloys' technological value. With features in modern devices already below 10 nm and designs capable of exploiting semimetals by confinement- and surface-assisted band gap engineering already proposed, the ability to further tune band gaps by controlling alloy composition introduces another dimension of customization exploitable in nanoelectronic designs.¹⁴⁻¹⁹

Fabrication of crystalline $\text{Ge}_{1-x}\text{Sn}_x$ alloys in the composition range predicted to exhibit semimetallic behavior when in bulk form has also been experimentally achieved. Recently, atomically flat epitaxial films grown on Ge(100) with tin content as high as $x = 0.46$ were reported in the

literature.²⁰ In their study, the high levels of compressive strain resulting from incorporation of such high tin content into films epitaxially constrained to germanium substrates resulted in maximum crystalline film thicknesses of 3 nm. In contrast, the use of lattice-matched substrates has been reported to allow growth of alloys with compositions $0.26 < x < 0.99$ and even stabilization of pure α -Sn films with thicknesses in excess of 100 nm;^{3,21–25} the reduction of strain associated with growth on lattice-matched substrates thus allows fabrication of semimetallic $\text{Ge}_{1-x}\text{Sn}_x$ with thicknesses on the order of hundreds of nanometers, which is well above the length scales required for modern nanoelectronics.

In this work we investigate the structural properties and thermodynamic stability of bulk and epitaxial $\text{Ge}_{1-x}\text{Sn}_x$ alloys. We employ density functional theory-based simulations in conjunction with the cluster expansion formalism in order to explore the relative stability of alloys across the full alloy composition range and devise strategies for maximizing the miscibility of germanium and tin.

II. METHODS

In order to assess the thermodynamic stability of $\text{Ge}_{1-x}\text{Sn}_x$ alloys across the concentration range we employ the Helmholtz free energy

$$F(x) = E(x) - TS(x), \quad (1)$$

where E is the internal energy, S the entropy, and both terms include vibrational, electronic, and configurational contributions. We describe the alloy in terms of an Ising model and compute the internal energy's configurational dependency by employing two levels of approximation: the Bragg-Williams model,^{26–28} and the cluster expansion formalism.²⁹

The Bragg-Williams (BW) model is a mean-field model in which the configurational energy of a substitutional alloy on an Ising lattice is described by nearest-neighbor interactions as

$$E_{\text{config}} = \sum_{i,j=\{\text{Ge},\text{Sn}\}} V_{ij} N_{ij}, \quad (2)$$

where V_{ij} and N_{ij} are the interaction energies (bond strengths) and number of bonds between species i and j , respectively. By assuming the alloy to be random—an assumption supported by experimental results^{–30,31} we may write the concentration-dependent energy per atom as

$$E_{\text{config}}(x) = (1-x)V_{\text{GeGe}} + xV_{\text{SnSn}} + 2x(1-x)V, \quad (3)$$

such that computing the alloy's configurational energy only requires knowledge of the interaction energies V_{ij} , which can be obtained from total energy calculations performed on crystalline structures (*e.g.* diamond or zinc-blende crystal structures). The sign and magnitude of

the *relative binding energy*

$$V = V_{\text{GeSn}} - \frac{1}{2}(V_{\text{GeGe}} + V_{\text{SnSn}}) \quad (4)$$

provide a quick and intuitive measure of the system's preference to either segregate or form a solid solution by comparing the energy of heteronuclear bonds with the average energy of homonuclear bonds. An improved description of the alloy's energetics can be achieved by employing a generalization of the model to include interactions beyond nearest neighbors: the cluster expansion formalism. By assigning spin-like occupation variables σ_i to sites i in the Ising lattice, we may expand the internal energy of an alloy with configuration $\sigma = \{\sigma_i\}$ as

$$E_{\text{config}}(\sigma) = \sum_{\alpha} J_{\alpha} \hat{S}_{\alpha}(\sigma), \quad (5)$$

where lattice sites are grouped into *clusters* α , \hat{S}_{α} is their associated pseudospin, and J_{α} their *effective cluster interactions* (ECI) (*i.e.* interaction energies). Since the magnitude of the ECI is found to decrease with cluster range, the internal energy of any configuration σ can be approximated by truncating the sum in eq. (5) to only include relatively compact clusters. The ECI in the truncated sum can then be determined from explicit total energy calculations performed on a relatively small set of configurations in an approach known as the structure inversion method or the Connolly-Williams method.³² In order to select the optimal set of crystalline structures and interactions to include when building the cluster expansion, we have employed the algorithm described in ref.³³.

The interaction energies required by both methods outlined above have been obtained employing density-functional theory (DFT) simulations within the usual Kohn-Sham framework in an implementation using norm-conserving pseudopotentials and linear combination of numerical atomic orbitals (NAO) basis sets.^{34–37} Basis sets used to expand wavefunctions include s4p4d3f2 NAO for germanium and s2p3d3f2 NAO for tin, where the notation indicates the number of *s*-type, *p*-type, *d*-type, and *f*-type orbitals centered about atoms of each species. Brillouin zone integrations are performed over a grid generated according to the Monkhorst-Pack³⁸ scheme maintaining a density of at least 7 k-points/Å^{–1}, whilst real-space quantities are discretized on a grid with a corresponding energy cut-off of at least 100 Ha. The local density approximation (LDA) was employed for the exchange-correlation potential.³⁹ Including spin-orbit interactions in our simulations was found to have a negligible effect on the structural properties and energetics of a selected set of alloy structures and has thus been neglected, similarly to another recent study on this alloy.¹⁰ Structural relaxations are performed on all simulated structures until forces acting on atoms are below 5×10^{-2} eV/Å and all stress tensor elements are below 0.1 GPa.

TABLE I. Structural parameters of germanium and tin’s α phase as computed with DFT-LDA in this work, and previously reported experimental values.

	a_0 (Å)		B_0 (GPa)	
	This work	Exp.	This work	Exp.
Ge	5.64	5.657 ⁴⁰	74	75.8 ⁴¹
Sn	6.47	6.489 ^{21,42}	47.16	42.5 – 53.1 ^{43,44}

The structural properties of tin and germanium’s diamond structures computed with this method are shown in table I. Within this approximation computed equilibrium lattice parameters show agreement with experimentally reported values to within 1%. While the bulk modulus computed for germanium exhibits a deviation of less than 3% with respect to experimentally reported values obtained via ultrasound, our computed bulk modulus for tin’s alpha phase lie within previously reported values obtained by fitting of neutron scattering data. Structural parameters for both alloy components are thus accurately described in our approximation.

Finite temperature effects are incorporated into our study by estimating contributions arising from vibrational and electronic degrees of freedom, as well as configurational contributions to entropy. Electronic contributions to free energy are computed within the one-electron and temperature-independent bands approximations by employing the electronic density of states computed within DFT.⁴⁵ Vibrational contributions are computed using the *bond stiffness versus bond length* approach whereby phonon frequencies in the alloy are estimated via a nearest-neighbor Born-von Kármán model with bond-length dependent force-constant tensors obtained by computing reaction forces on crystalline structures perturbed with strain and atomic displacements.^{46,47} Configurational entropy has been estimated from Boltzmann’s expression by accounting for all possible ways of arranging atoms in a cell given its composition. Computed configurational, electronic, and vibrational contributions have been combined and temperature-dependent ECI have been generated, allowing finite-temperature free energy simulations to be performed in larger cells with dimensions on the order of hundred of nanometers with with relatively low computational effort.

The phase boundary between ordered and disordered states with varying temperature has been obtained across the composition range via Monte Carlo (MC) simulations. MC simulations employing the described lattice model and cluster expansion ECI have been performed on simulation cells with dimensions of at least 150 nm in order to include long-range interactions and accurately trace the boundary between low-temperature ordered states and high-temperature random alloys using the procedure and implementation described in ref.⁴⁸.

We complement our cluster expansion results by directly exploring the properties of random alloys using

DFT through the use of Special Quasirandom Structures (SQS). SQS represent a periodic supercell approximation to random alloys by targeting multisite correlations characteristic of the disordered state, thus enabling *ab-initio* simulations on such systems.^{49,50} We have employed a set of 64-atom SQS generated by targeting disordered-state pair and triplet correlations with ranges up to a nanometer; structures covering the full composition range were generated using the algorithm and implementation described in refs.^{45,51}.

III. RESULTS AND DISCUSSION

A. Bulk alloys

The configurational dependence of the random alloy’s energy across the composition range is estimated in a first approximation within the Bragg-Williams model by obtaining nearest-neighbor interaction energies as the formation energy per bond of germanium and tin’s α phase, and an $x = 0.5$ alloy in a zincblende structure. Resulting interaction energies predict a positive relative binding energy $V_{\text{GeSn}} = 11$ meV, indicating the alloy’s preference to segregate at zero temperature.

A more accurate description of alloy energetics has been obtained by fitting the energy of 47 crystalline structures with up to 8 atoms per cell to a cluster expansion including pairs with atoms up to 1 nm apart, and triplets with ranges up to 0.52 nm. Figure 1(a) shows fitted values of effective cluster interactions, where we observe coefficients to decay rapidly with cluster diameter and number of sites in the cluster from around 20 meV/atom for nearest-neighbor pairs down to less than 5 meV/atom for longer range pairs and even lower values associated to triplets included in the fit. The CE cross-validation score – a measure of its predictive power analogous to the root mean square error^{–52} is 5 meV/atom, indicating a level of accuracy similar to that of DFT simulations used in the construction of the fit. In accordance with observed experimental behavior and results from the BW model, CE results predict germanium and tin to be immiscible at zero temperature as no ordered structures were found to be energetically favorable with respect to segregation into each of the component’s α phase across the entire composition range, as shown in fig. 1(b).

Results obtained with lattice models are complemented with directly computed quantities employing *ab-initio* simulations of 64-atom SQS. Atomic positions and lattice vectors in generated SQS have been relaxed using DFT under a scheme that constrains the cell shape whilst allowing cell volume and atomic positions to vary; this procedure provides the most accurate representation of the disordered state by not allowing macroscopic anisotropy in cell shape relaxations.⁵³ The difference in atomic radii results in structures where relaxed atomic positions exhibit root-mean-square deviations from ideal lattice sites of up to 0.157 nm away for $x = 0.5$. Their structural

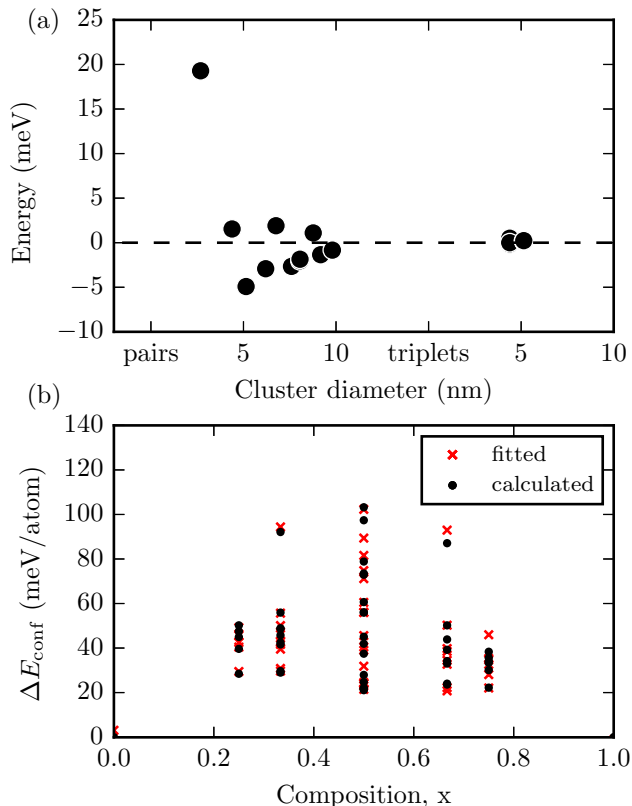


FIG. 1. (a) Magnitude of effective cluster interactions (ECI) obtained in the cluster expansion fit for bulk alloys and (b) predicted and directly computed formation energies per atom for all structures included in the fit.

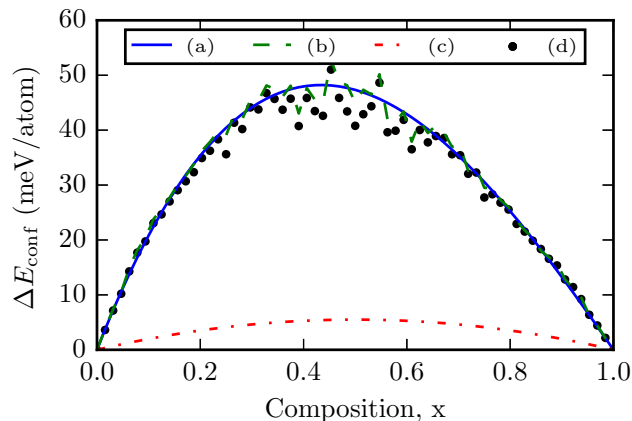


FIG. 2. Formation energy of mixing at zero temperature of (a) random alloys and (b) *quasi*-random alloys as predicted by the cluster expansion; (c) random alloys as predicted by the BW model, and (d) 64-atom SQS as predicted by DFT simulations.

properties are compared to available literature by fitting their equilibrium lattice constant across the composition range to

$$a_0^{\text{Ge}_{1-x}\text{Sn}_x} = a_0^{\text{Ge}}(1-x) + a_0^{\text{Sn}}x + b_a x(1-x), \quad (6)$$

where we have obtained a bowing parameter value of $b_a = 0.056 \text{ \AA}$, in agreement with values reported in recent theoretical and experimental works.^{4,10,54} Figure 2 shows the formation energy per atom of random alloys with respect to spinodal decomposition across the concentration range as predicted with the Bragg-Williams model, the cluster expansion, and as directly computed with DFT simulations of structurally optimized SQS. We observe that although the BW model correctly predicts immiscibility, it significantly underestimates the formation energy of random alloys compared to results obtained with CE and SQS. The higher accuracy and predictive power of the CE is reflected by its significantly smaller deviations away from formation energies directly computed with DFT using SQS, where an RMS error of 2 meV/atom between both datasets has been computed. We additionally plot the CE predicted formation energies for *quasi*-random structures with site correlations corresponding to those of generated SQS; the closer tracking of SQS formation energies by this curve—especially around intermediate compositions, where larger deviations are found—highlights the impact of imposed periodicity on SQS energetics.

We extend our model to finite temperatures by estimating the magnitude of configurational, electronic, and vibrational entropy contributions to alloy free energy. Electronic entropy has been estimated employing the electronic density of states computed with DFT for SQS across the full composition range: contributions to alloy free energy have been found to be negligible with computed values below 1 meV/atom at temperatures up to 1000 K across the entire concentration range, as expected for non-metallic alloys. Electronic entropy contributions to free energy have not been included in results presented in the remainder of this work.

Free energy contributions arising from vibrational degrees of freedom have been estimated by fitting the components of a nearest-neighbor force constant tensor to reaction forces on crystalline structures with small atomic displacements and for varying degrees of strain. Vibrational entropy contributions for random alloys across the composition range have then been computed employing phonon frequencies associated with bond length distributions in structurally optimized SQS cells.

The relative magnitude of entropy contributions included are explored through results directly obtained for SQS cells. Figure 3 shows the temperature dependence of the free energy of mixing for structures at compositions of $x = 0.25, 0.5,$ and 0.75 : configurational contributions dominate alloy stabilization while vibrational entropy of mixing contributes to a lesser degree with values around an order of magnitude lower at temperatures above 200 K in compositions shown in the figure. We

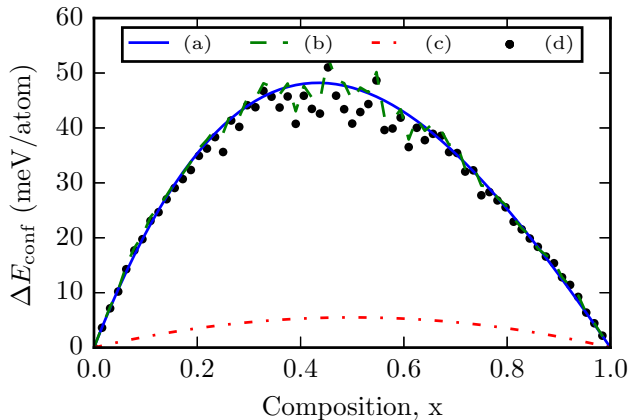


FIG. 3. Temperature dependence of the total free energy of mixing and considered contributions as estimated for 64-atom SQS for (a) $x = 0.25$, (b) $x = 0.50$, and (c) $x = 0.75$ alloy compositions.

observe predicted critical temperatures –i.e. temperatures at which the disordered phase becomes energetically favorable– to decrease for larger tin compositions in a result attributable to the asymmetry observed in the alloy’s configurational energy of mixing ΔE_{conf} (see fig. 2). While this asymmetry in formation energy with composition is also predicted by the CE fit, the BW model’s lack of triplet interactions fails to reproduce it. We further investigate the origin of this feature in alloy energetics by decomposing the computed energy of mixing as:

$$\Delta E_{\text{conf}} = \Delta E_{VD} + \delta E_{UR}^{\text{chem}} + \delta E^{\text{int}}, \quad (7)$$

where the *volume deformation* energy ΔE_{VD} corresponds to the energy required to hydrostatically strain each of the constituents to the alloy’s equilibrium lattice parameter, the *chemical* or *spin-flip* energy $\delta E_{UR}^{\text{chem}}$ corresponds to the energy gained when both components already strained bond together to form the alloy, and the *internal relaxation* energy δE^{int} is the energy gained when atomic positions in the alloy are allowed to relax. Figure 4 shows the magnitude of each contribution in quasi-random alloys as computed for 64-atom SQS with compositions $x=0.25$, $x=0.50$, and $x=0.75$. The large difference between both components’ equilibrium lattice parameter results in the volume deformation energy being the single largest contribution to mixing enthalpy and main source of alloy destabilization. Contributions arising from chemical interactions between different atomic species and the relaxation of internal coordinates are of similar magnitude and act to stabilize the alloys, partially counteracting the effects of volume deformation. Table II lists the the magnitude of each contribution for three alloy compositions: the difference in components’ bulk moduli introduces an asymmetry in alloy energetics and results in larger *volume deformation* contributions –and thus decreased stability– in germanium-rich alloys

Composition (x)	ΔE_{conf}	ΔE_{VD}	$\delta E_{UR}^{\text{chem}}$	δE^{int}
	(meV/atom)			
0.25	36	192	-88	-67
0.50	41	207	-90	-76
0.75	28	128	-52	-48

TABLE II. Formation energy of mixing decomposition into contributions listed in eq. (7) for bulk alloys with varying composition.

when compared to tin-rich alloys. While stabilizing chemical and internal relaxation contributions also exhibit larger magnitudes for germanium-rich alloys their smaller magnitude does not offset the destabilizing asymmetry, resulting in an increased energetic stability of alloys on the tin-rich side of the composition range.

We explore the effects of this asymmetry on the system’s critical temperature by tracing the phase boundary between the disordered phase and decomposition into elemental α phases by combining the obtained CE fit with a lattice model Monte Carlo (MC) simulation. MC simulations of lattice models represent an accurate method to compute thermodynamic properties of substitutional alloys. These methods extend beyond the capabilities of first-principles calculations by allowing the simulation of cells with sizes on the order of hundreds of nanometers, thus enabling the inclusion of long-range interactions impractical to include in smaller *ab-initio* simulations cells. We include the effects of vibrational degrees of freedom by fitting contributions obtained for SQS cells across the full composition range to temperature-dependent ECIs incorporating both the effects of configurational and vibrational degrees of freedom.

The phase diagram for the $\text{Ge}_{1-x}\text{Sn}_x$ system calculated via MC lattice model is shown in fig. 5. Critical temperatures obtained with this method by only including configurational degrees of freedom are significantly higher than those predicted using SQS cells. This result is presumably due to a combination of the latter’s deviations of site correlations from those of random alloys, and the omission of long-range interactions inherent in the use of smaller cells required to maintain tractability for *ab-initio* simulations. Inclusion of vibrational degrees of freedom reduces predicted critical temperatures with a more pronounced effect on the germanium-rich side of the composition range. This indicates the stabilization associated with the softening of phonon modes in the material by addition of tin partially counteracts the decreased stability associated with the compression of germanium bond lengths.

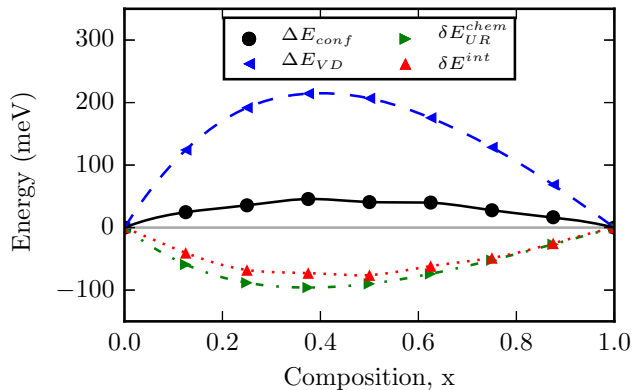


FIG. 4. Formation energy of mixing decomposition obtained from DFT simulations of bulk alloys employing SQS.

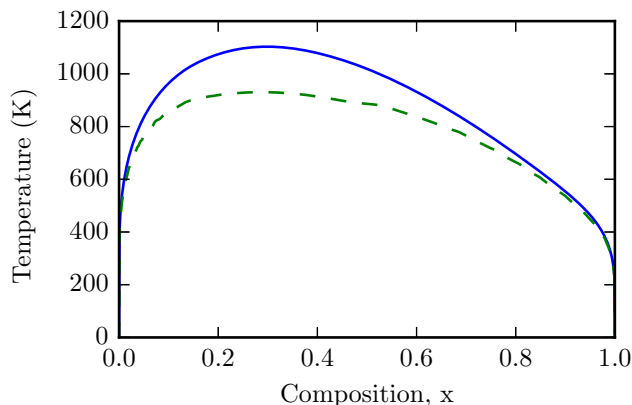


FIG. 5. Phase diagram of bulk alloys as calculated employing CE fits constructed including (dashed line) and excluding (solid line) vibrational degrees of freedom. Regions above the lines represent stability of random alloys.

B. Epitaxial alloys

Predicted critical temperatures for bulk alloys at intermediate compositions shown in fig. 5 are well above tin’s melting temperature and even near germanium’s, indicating growth of bulk $\text{Ge}_{1-x}\text{Sn}_x$ alloys is not possible at ambient pressure.⁵⁵ Since the main contribution to such high critical temperatures has been found to arise from the large difference in volume between components, we explore the effects of coherent epitaxial growth on alloy energetics as a way of reducing forces driving destabilization by constraining the lattice spacing of the alloy—and thus of the potentially segregating components—along the plane defined by the substrate surface in a phenomenon known as *epitaxial stabilization*.^{56–58}

To investigate how tin-germanium alloys can be stabilized by epitaxial growth of thin films, we simulate SQS cells with a crystallographic plane constrained to lattice spacing corresponding to substrates which

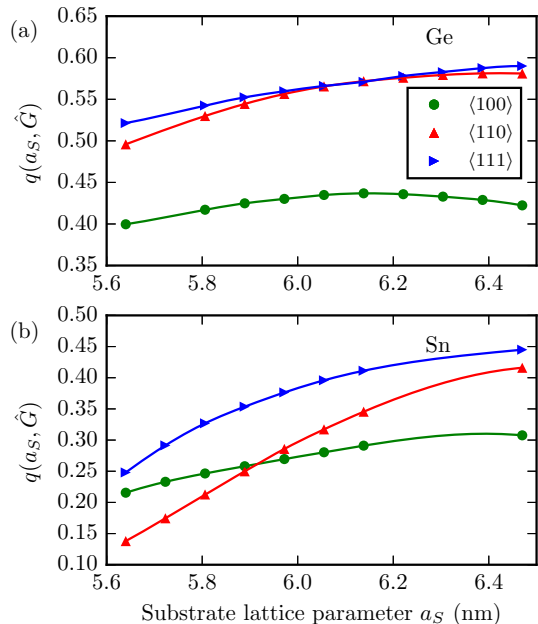


FIG. 6. Epitaxial softening functions for (a) Ge and (b) Sn as computed employing DFT simulations.

have been previously employed for growing epitaxially stable films of α -Sn and/or germanium-tin alloys: Ge (5.64Å), ZnTe/GaSb (6.10Å), and CdTe/InSb (6.48Å).^{3,21,24,25,59,60}

In order to select a crystallographic plane along which to simulate growth we compute the *epitaxial softening function* of both germanium and tin as

$$q(a_S, \hat{G}) = \frac{\Delta E^{epi}(a_S, \hat{G})}{\Delta E^{bulk}(a_S)}, \quad (8)$$

which gives the ratio between the epitaxial increase in energy due to biaxial strain to a particular substrate lattice constant a_S along a plane perpendicular to direction \hat{G} , and the hydrostatic increase in energy due to triaxial strain to the same a_S . This dimensionless parameter quantifies the degree of out-of-plane relaxation exhibited by a material grown epitaxially; it is desirable to minimize $q(a_S, \hat{G})$ (and thus $\Delta E^{epi}(a_S, \hat{G})$) for a given substrate in order to avoid or reduce dislocations and other strain-induced film/surface defects.⁶¹ Figure 6 shows the epitaxial softening functions of germanium and tin as computed with DFT, where we observe (100) to be the softest direction for both constituents around their equilibrium lattice constant, and for alloys across the composition range if we approximate their epitaxial softening function as the corresponding weighted sum. We thus find that (100)-oriented substrates minimize strain energy and thus structural defects on epitaxially coherent $\text{Ge}_{1-x}\text{Sn}_x$ films, in agreement with experimental literature.⁶²

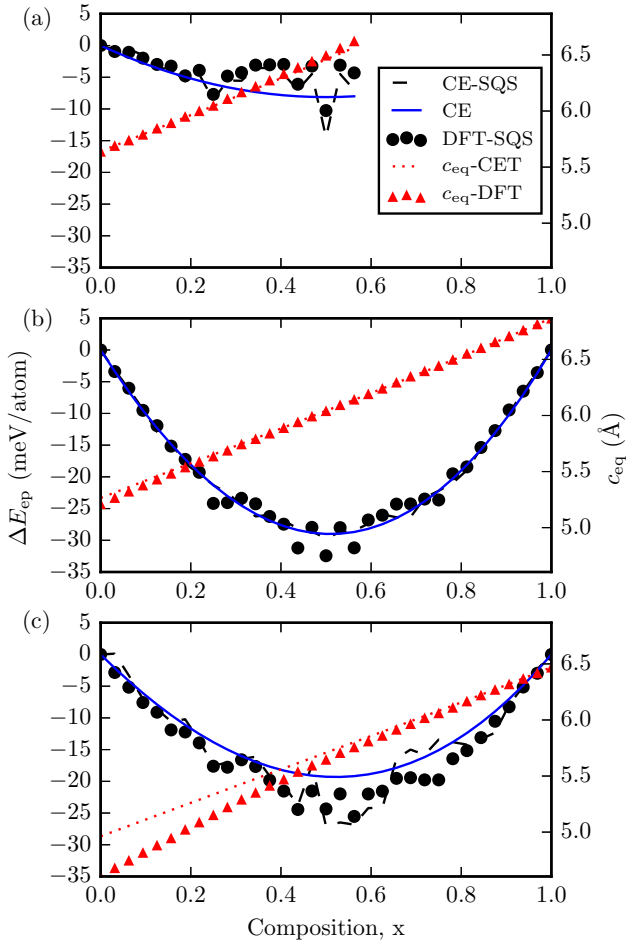


FIG. 7. Formation energy of mixing with respect to coherent decomposition and out-of-plane equilibrium cell parameter c_{eq} for alloys grown on (a) Ge, (b) ZnTe/GaSb, and (c) CdTe/InSb.

We simulate epitaxial growth on (100)-oriented substrates by constraining 64-atom SQS along two of their $\langle 100 \rangle$ directions to match the lattice spacing of each of the proposed substrates while allowing the cell to relax along the perpendicular direction. While this scheme neglects the potentially large role of surfaces and interfaces inherently present around thin films, it provides an energetic baseline and thus insight into the stability of epitaxially alloys independent of surface effects and for portions of the material deep into coherently grown films with thicknesses greater than a few tens of nanometer, once surface effects have been screened. Figure 7 shows the computed epitaxial formation energy relative to coherent decomposition of its constituents; we observe how the strain-induced destabilization of constituent segregation imposed by epitaxial coherency results in the stabilization of alloys even at zero temperature. Structural relaxation simulations of alloys constrained to Ge(100) substrates with compositions above $x = 0.56$ resulted in amorphous structures and have thus been

excluded from presented results. Formation energies obtained from *ab-initio* simulations have been fitted to CEs with the corresponding symmetry in order to investigate the case of random alloys and eliminate variations due to deviations in site correlations springing from the use of periodic cells. The CE fits predict all alloys to be energetically favorable with respect to coherent decomposition, with results showing a trend where stability decreases along the (ZnTe/GaSb)-(CdTe/InSb)-Ge sequence, indicating growth on germanium to be the least favorable choice. Additionally, Figure 7 also shows the magnitude of the out-of-plane lattice parameter c_{eq} for each substrate as computed with SQS-DFT, and as predicted by continuum elasticity theory (CET)⁵⁷ where good agreement between both methods is obtained across most of the composition range in Ge and ZnTe/GaSb substrates, and significant deviations are observed for low tin content alloys coherent with CdTe/InSb substrates.

Decompositions of epitaxial formation energies akin to those defined for bulk alloys in eq. (7) are presented in table III for alloys with composition $x = 0.5$. The effects of growth on lattice-matched substrates can be observed in the formation energy decomposition corresponding to ZnTe/GaSb substrates: while computed epitaxial spin-flip ($\delta E_{UR}^{chem,epi}$) and internal relaxation ($\delta E_{UR}^{int,epi}$) energies remain the same as in the corresponding bulk alloy, volume deformation energy relative to epitaxially coherent decomposition ΔE_{VD}^{epi} is reduced by 37%, resulting in significantly enhanced stability. By comparing results across substrates we observe that while destabilization of component segregation results in an overall reduction of ΔE_{VD}^{epi} with increasing substrate lattice parameter due to germanium's larger bulk modulus, the magnitudes of stabilizing contributions $\delta E_{UR}^{chem,epi}$ and $\delta E_{UR}^{int,epi}$ are observed to also decrease with increasing bond lengths associated with alloys grown on substrates with larger lattice spacings.

Finally, we compare the relative stability of alloys grown on different substrates in fig. 8 by computing epitaxial alloys' formation energies with respect to spinodal decomposition into their bulk components. The *substrate* providing the lowest formation energy (and thus highest stability with respect to non-coherent decomposition) is observed to depend on alloy composition. Within the considered set of substrates, Ge is preferred for compositions below $x = 0.25$, CdTe/InSb for compositions above $x = 0.76$, and ZnTe/GaSb for $0.25 < x < 0.76$, indicating the latter to be energetically favorable across most of the composition range where the alloy exhibits semimetallic behavior. The asymmetry discussed for bulk alloys whereby tin-rich compositions exhibit increased stability is also present for alloys grown on ZnTe/GaSb, as can be clearly seen in fig. 8.

Substrate	$\Delta E_{\text{conf}}^{\text{epi}}$	$\Delta E_{\text{VD}}^{\text{epi}}$	$\delta E_{\text{UR}}^{\text{chem,epi}}$	$\delta E^{\text{int,epi}}$
		(meV/atom)		
Ge	-10	195	-107	-97
ZnTe/GaSb	-32	131	-89	-75
CdTe/InSb	-24	114	-76	-62

TABLE III. Epitaxial formation energy of mixing decomposition for alloys with composition $x = 0.5$ grown on each of the substrates included in this study.

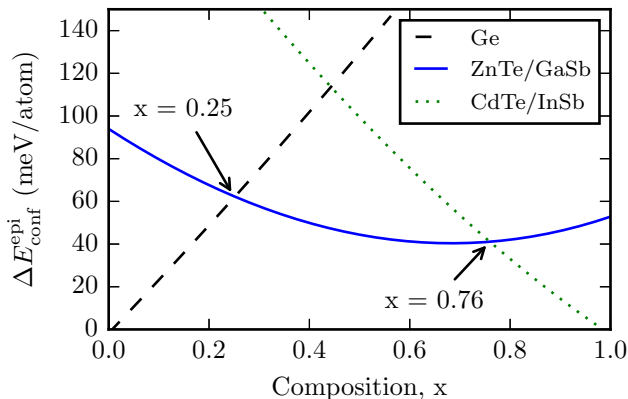


FIG. 8. Formation energy of mixing of epitaxially grown alloys with respect to decomposition into bulk components.

IV. CONCLUSION

The thermodynamics of tin germanium alloys have been studied using a cluster expansion (CE) approach parametrized from first principle DFT simulations. The nearest neighbor version of the CE (the BW model) for a random alloy correctly predicts tin and germanium to be immiscible across the full concentration range at zero temperature. Inclusion of clusters with higher order and longer range into the expansion dramatically improves agreement with first principle simulations, both in terms of magnitude and an asymmetric skew observed in alloy formation energies as a function of alloy composition. It is found that including pair interactions with ranges of up to a nanometer and triplet interactions up to around half a nanometer is sufficient to describe the energetics of bulk alloys. Temperature effects on free energy are included by adding configurational, electronic, and vibrational entropies. Electronic entropy contributions are estimated from a one electron approximation and by considering band energies to be independent of temperature, and contributions arising from vibrational degrees of freedom to both entropy and internal energy (zero-point energy) are estimated from bond stiffness versus

bond length approximation. Free energy contributions arising from electronic degrees of freedom are found to be negligible and are expected to only weakly influence the alloys' thermodynamics. It is shown that the critical temperature for stability of random alloys generally decreases for higher Sn concentrations as a result of an asymmetry in the mixing enthalpy; decomposition of the latter into a volume deformation term related to each element's elastic properties, a chemical energy term related to bond strengths, and an internal relaxation energy. The volume deformation term dominates the zero-temperature mixing enthalpy and severely reduces the stability of bulk alloys, although it is partially counteracted by the stabilizing effects of the chemical and relaxation energies. The large volume deformation energies results in predicted critical temperatures that are higher than the melting temperature of Sn and are only slightly lower than the melting temperature for Ge.

After identifying the volume deformation energy as the largest contribution towards destabilization of bulk alloys, the influence of biaxial strain due to coherent epitaxial growth is considered for different substrates which have been previously employed to grow germanium-tin alloys. The role of epitaxial stabilization on the free energy is considered for three substrates: Ge (5.64Å), ZnTe/GaSb (6.10Å), and CdTe/InSb (6.48Å). These three substrates allow for lattice matching for compositions of $x=0$, and approximately for $x=0.5$ and $x=1$, respectively. The preferred orientation for epitaxial growth on the substrates is investigated using the epitaxial softening function as a measure. It is found that epitaxial films grown on (001)-oriented substrates are best able to minimize strain in the alloy by relaxation in the direction normal to the film's surface. The destabilization of components segregation due to epitaxial constraints in tandem with appropriate choice of substrate and growth orientation tends to stabilize the films, enabling growth of alloys that are unstable in bulk form. Hence guidelines and strategies for growth of germanium tin can be approached from the viewpoint of stabilizing the alloy by reducing the volume deformation energy and restricting segregation of components. Against this backdrop, growth of tin-rich alloys on lattice-matched substrates thus maximizes stability of epitaxial germanium tin. Although bulk tin-rich alloys have been predicted to exhibit semimetallic behavior, the electronic structure character of thin films may be altered by quantum size effects and thus render them intriguing and potentially useful for applications in electronic devices.

ACKNOWLEDGMENTS

This work was funded by Science Foundation Ireland through a Principal Investigator award Grant No. 13/IA/1956.

- * Jim.Greer@nottingham.edu.cn
- 1 U. Mizutani, *Hume-Rothery Rules for Structurally Complex Alloys* (CRC Press, 2010).
 - 2 G. V. Raynor and R. W. Smith, Proceedings of the Royal Society of London. Series A, Mathematical and Physical Sciences **391**, 323 (1982).
 - 3 J. Piao, R. Beresford, T. Licata, W. Wang, and H. Homma, Journal of Vacuum Science & Technology B: Microelectronics Processing and Phenomena **8**, 221 (1990).
 - 4 F. Gencarelli, B. Vincent, J. Demeulemeester, A. Vantomme, A. Moussa, A. Franquet, A. Kumar, H. Bender, J. Meersschaut, W. Vandervorst, R. Loo, M. Caymax, K. Temst, and M. Heyns, ECS Transactions **50**, 875 (2013).
 - 5 S. Wirths, D. Buca, and S. Mantl, Progress in Crystal Growth and Characterization of Materials **62**, 216 (2016).
 - 6 W. Dou, M. Benamara, A. Mosleh, J. Margetis, P. Grant, Y. Zhou, S. Al-Kabi, W. Du, J. Tolle, B. Li, *et al.*, Scientific reports **8**, 5640 (2018).
 - 7 S. Wirths, R. Geiger, N. von den Driesch, G. Mussler, T. Stoica, S. Mantl, Z. Ikonic, M. Luysberg, S. Chiussi, J. M. Hartmann, H. Sigg, J. Faist, D. Buca, and D. Grützmacher, Nature Photonics **9**, 88 (2015).
 - 8 V. Reboud, A. Gassenq, N. Pauc, J. Aubin, L. Milord, Q. Thai, M. Bertrand, K. Guilloy, D. Rouchon, J. Rothman, *et al.*, Applied Physics Letters **111**, 092101 (2017).
 - 9 D. Rainko, Z. Ikonic, A. Elbaz, N. von den Driesch, D. Stange, E. Herth, P. Boucaud, M. E. Kurdi, D. Grtzmacher, and D. Buca, Scientific Reports **9** (2019), 10.1038/s41598-018-36837-8.
 - 10 M. P. Polak, P. Scharoch, and R. Kudrawiec, Journal of Physics D: Applied Physics **50**, 195103 (2017).
 - 11 J. D. Sau and M. L. Cohen, Physical Review B **75** (2007), 10.1103/physrevb.75.045208.
 - 12 K.-H. Kao, A. S. Verhulst, W. G. Vandenberghe, B. Soree, G. Groeseneken, and K. D. Meyer, IEEE Transactions on Electron Devices **59**, 292 (2012).
 - 13 C. Schulte-Braucks, D. Stange, N. von den Driesch, S. Blaeser, Z. Ikonic, J. M. Hartmann, S. Mantl, and D. Buca, Applied Physics Letters **107**, 042101 (2015).
 - 14 L. Ansari, G. Fagas, J.-P. Colinge, and J. C. Greer, Nano Letters **12**, 2222 (2012).
 - 15 A. Sanchez-Soares and J. C. Greer, Nano Letters **16**, 7639 (2016).
 - 16 L. Ansari, G. Fagas, F. Gity, and J. C. Greer, Applied Physics Letters **109**, 063108 (2016).
 - 17 A. Sanchez-Soares, C. O'Donnell, and J. C. Greer, Physical Review B **94** (2016), 10.1103/physrevb.94.235442.
 - 18 F. Gity, L. Ansari, M. Lanius, P. Schüffelgen, G. Mussler, D. Grützmacher, and J. C. Greer, Applied Physics Letters **110**, 093111 (2017).
 - 19 F. Gity, L. Ansari, C. König, G. A. Verni, J. D. Holmes, B. Long, M. Lanius, P. Schüffelgen, G. Mussler, D. Grützmacher, *et al.*, Microelectronic Engineering **195**, 21 (2018).
 - 20 A. Suzuki, O. Nakatsuka, S. Shibayama, M. Sakashita, W. Takeuchi, M. Kurosawa, and S. Zaima, Japanese Journal of Applied Physics **55**, 04EB12 (2016).
 - 21 R. Farrow, D. Robertson, G. Williams, A. Cullis, G. Jones, I. Young, and P. Dennis, Journal of Crystal Growth **54**, 507 (1981).
 - 22 H. Hochst and I. Hernandez-Calderon, Surface Science **126**, 25 (1983).
 - 23 M. Tsom, E. A. Fitzgerald, A. R. Kortan, B. Spear, and L. C. Kimerling, Applied Physics Letters **55**, 578 (1989).
 - 24 P. John, T. Miller, and T.-C. Chiang, Physical Review B **39**, 3223 (1989).
 - 25 R. C. Bowman, P. M. Adams, M. A. Engelhart, and H. Hchst, Journal of Vacuum Science & Technology A: Vacuum, Surfaces, and Films **10**, 1000 (1992).
 - 26 W. L. Bragg and E. J. Williams, Proceedings of the Royal Society A: Mathematical, Physical and Engineering Sciences **244**, 101 (1958).
 - 27 E. Williams, Proceedings of the Royal Society of London. Series A, Mathematical and Physical Sciences **151**, 231 (1935).
 - 28 E. Williams, Proceedings of the Royal Society of London. Series A, Mathematical and Physical Sciences **152**, 231 (1935).
 - 29 J. M. Sanchez, F. Ducastelle, and D. Gratias, Physica A. Statistical and Theoretical Physics **128**, 334 (1984).
 - 30 S. Biswas, J. Doherty, D. Saladukha, Q. Rammase, D. Majumdar, M. Upmanyu, A. Singha, T. Ochalski, M. A. Morris, and J. D. Holmes, Nature Communications **7** (2016), 10.1038/ncomms11405.
 - 31 S. Mukherjee, N. Kodali, D. Isheim, S. Wirths, J. M. Hartmann, D. Buca, D. N. Seidman, and O. Moutanabbir, Physical Review B **95** (2017), 10.1103/physrevb.95.161402.
 - 32 J. W. D. Connolly and A. R. Williams, Physical Review B **27**, 5169 (1983).
 - 33 A. Van De Walle, M. Asta, and G. Ceder, Calphad **26**, 539 (2002).
 - 34 J. M. Soler, E. Artacho, J. D. Gale, A. García, J. Junquera, P. Ordejón, and D. Sánchez-Portal, Journal of Physics: Condensed Matter **14**, 2745 (2002).
 - 35 T. Ozaki, Phys. Rev. B **67**, 155108 (2003).
 - 36 T. Ozaki and H. Kino, Phys. Rev. B **69**, 195113 (2004).
 - 37 Atomistix Toolkit version 2016.4, "QuantumWise A/S (www.quantumwise.com).".
 - 38 H. J. Monkhorst and J. D. Pack, Phys. Rev. B **13**, 5188 (1976).
 - 39 J. P. Perdew and A. Zunger, Physical Review B **23**, 5048 (1981).
 - 40 J. F. C. Baker and M. Hart, Acta Crystallographica Section A **31**, 364 (1975).
 - 41 L. J. Bruner and R. W. Keyes, Physical Review Letters **7**, 55 (1961).
 - 42 J. Thewlis and A. Davey, Nature **174**, 1011 (1954).
 - 43 D. L. Price, J. M. Rowe, and R. M. Nicklow, Physical Review B **3**, 1268 (1971).
 - 44 C. Buchenauer, M. Cardona, and F. Pollak, Physical Review B **3**, 1243 (1971).
 - 45 A. van de Walle, Calphad **33**, 266 (2009).
 - 46 A. van de Walle and G. Ceder, Reviews of Modern Physics **74**, 11 (2002).
 - 47 B. Fultz, Progress in Materials Science **55**, 247 (2010).
 - 48 A. van de Walle and M. Asta, Modelling and Simulation in Materials Science and Engineering **10**, 52 (2012).
 - 49 A. Zunger, S.-H. Wei, L. Ferreira, and J. E. Bernard, Physical Review Letters **65**, 353 (1990).
 - 50 K. Hass, L. Davis, and A. Zunger, Physical Review B **42**, 3757 (1990).
 - 51 A. Van de Walle, P. Tiwary, M. De Jong, D. Olmsted, M. Asta, A. Dick, D. Shin, Y. Wang, L.-Q. Chen, and

- Z.-K. Liu, *Calphad* **42**, 13 (2013).
- ⁵² A. van de Walle and G. Ceder, *Journal of Phase Equilibria* **23**, 348 (2002).
- ⁵³ G. Ghosh, A. van de Walle, and M. Asta, *Acta Materialia* **56**, 3202 (2008).
- ⁵⁴ R. Beeler, R. Roucka, A. V. G. Chizmeshya, J. Kouvetakis, and J. Menéndez, *Physical Review B* **84** (2011), 10.1103/physrevb.84.035204.
- ⁵⁵ R. W. Olesinski and G. J. Abbaschian, *Bulletin of Alloy Phase Diagrams* **5**, 265 (1984).
- ⁵⁶ D. M. Wood and A. Zunger, *Physical Review Letters* **61**, 1501 (1988).
- ⁵⁷ A. Zunger and D. Wood, *Journal of Crystal Growth* **98**, 1 (1989).
- ⁵⁸ V. Ozoliņš, C. Wolverton, and A. Zunger, *Physical Review B* **57**, 4816 (1998).
- ⁵⁹ C. A. Hoffman, J. R. Meyer, R. J. Wagner, F. J. Bartoli, M. A. Engelhardt, and H. Höchst, *Physical Review B* **40**, 11693 (1989).
- ⁶⁰ E. Calavita, M. A. Engelhart, and Höchst, in *The Physics of Semiconductors: Proceedings of the 20th International Conference* (1990).
- ⁶¹ V. Ozoliņš, C. Wolverton, and A. Zunger, *Applied Physics Letters* **72**, 427 (1998).
- ⁶² T. Asano, S. Kidowaki, M. Kurosawa, N. Taoka, O. Nakatsuka, and S. Zaima, *Thin Solid Films* **557**, 159 (2014).